

INVESTIGATION OF BLOOD-LIKE NON-NEWTONIAN FLUID FLOW IN STENOTIC ARTERIES USING THE LATTICE BOLTZMANN METHOD IN 2D

KATEŘINA ŠKARDOVÁ*, PAVEL EICHLER*, TOMÁŠ OBERHUBER*, AND RADEK
FUČÍK*

Abstract. The impact of non-Newtonian fluid properties on the mathematical modeling of flow in stenosed arteries is investigated. The main goal is to determine whether the Newtonian fluid model is sufficient for the flow modeling in the desired geometry. The magnitude of negative horizontal flux is used as a primary quantity for comparing Newtonian and non-Newtonian approaches. The comparison is performed for vessel geometries with gradually increasing severity of stenosis. The mathematical model is solved using the lattice Boltzmann method with a modification to include the non-Newtonian effects. The results show that the difference in fluid characteristics increases with the degree of stenosis. However, for the simulation of flow in the least stenosed artery, both models provide similar results and, thus, the Newtonian model can be employed.

Key words. computational fluid dynamics, non-Newtonian fluid, cascaded lattice Boltzmann method, vessel stenosis

AMS subject classifications. 76D99, 65Z05, 65M99

1. Introduction. The investigation of blood flow characteristics using the mathematical modelling can contribute to a better interpretation of correlations between the regions of turbulent flow, shear stress on the artery walls, and other patterns contributing to cardiovascular diseases. As shown in [5], the investigation of pathologies in such vessels using the magnetic resonance imaging (MRI) flow measurement is often underestimated due to the presence of a significant backflow induced by turbulence. It is well known that blood behaves as a pseudoplastic fluid for low strain rates and as Newtonian for high strain rates, i.e., in large vessels such as arterial vessels [9]. The objective of this study is to determine under which conditions the blood flow can be considered as Newtonian in a simplified, two-dimensional geometry of a large vessel. This is done by comparing the magnitude of backflow for both Newtonian and non-Newtonian mathematical models in a vessel with various degrees of stenosis or coarctation.

To investigate the non-Newtonian fluid behavior in the arterial vessel geometry, numerical simulations using the lattice Boltzmann method (LBM) are used. The LBM is a numerical method for the solution of the incompressible Navier-Stokes equations [11]. In last decades, the method has been intensively studied by many researchers and there exist several variants of LBM such as the Single Relaxation Time LBM [8], Multiple Relaxation Times LBM [3], Cascaded LBM [6], Cumulant LBM [7], Entropic LBM [2], and others. Because some LBM variants suffer from instabilities for higher Reynolds number flows, the Cascaded LBM (CLBM) is used in this work [6].

The work is organized as follows. In Section 2, the mathematical model is summarized and the numerical model is introduced. Then, in Section 4, results of the non-Newtonian and Newtonian fluid flow simulations are presented and discussed. The last section concludes the observations.

*Department of Mathematics, Faculty of Nuclear Sciences and Physical Engineering, Czech Technical University in Prague, Trojanova 13, 120 00 Praha 2.

2. Mathematical model. The dynamics of the incompressible fluid in a rectangular domain $\Omega = (0, L_x) \times (0, L_y)$, L_x, L_y [m] and within the time interval $(0, T_{fin})$, T_{fin} [s], can be described by the following balance equations:

$$\nabla \cdot \vec{u} = 0, \quad (2.1)$$

$$\rho \left(\frac{\partial \vec{u}}{\partial t} + \vec{u} \cdot \nabla \vec{u} \right) + \nabla p = \nabla \cdot \mathbb{T}_\mu + \rho \vec{g}, \quad (2.2)$$

where ρ [kg m^{-3}] denotes the fluid density, \vec{u} [m s^{-1}] denotes the fluid velocity, p [$\text{kg m}^{-1} \text{s}^{-2}$] is the pressure, \mathbb{T}_μ [$\text{kg m}^{-1} \text{s}^{-2}$] denotes the viscous stress tensor, and \vec{g} [m s^{-2}] is the acceleration caused by external forces.

Under the assumption that the non-Newtonian fluid in question is an incompressible, generalized Newtonian fluid, the viscous stress tensor \mathbb{T}_μ is given by

$$\mathbb{T}_\mu = 2\mu \mathbb{D}, \quad (2.3a)$$

where μ [$\text{kg m}^{-1} \text{s}^{-1}$] is the apparent dynamic viscosity and

$$\mathbb{D} = \frac{1}{2} (\nabla \vec{u} + (\nabla \vec{u})^T). \quad (2.3b)$$

Moreover, assumption of small variations of viscosity, i.e., $\nabla \mu \approx 0$, allows to express Eq. (2.2) as

$$\rho \left(\frac{\partial \vec{u}}{\partial t} + \vec{u} \cdot \nabla \vec{u} \right) + \nabla p = 2\mu \nabla \cdot \mathbb{D} + \rho \vec{g}. \quad (2.4)$$

For the generalized Newtonian fluid, the apparent dynamic viscosity is a function of the shear rate $\dot{\gamma}$ [s^{-1}] defined using the Frobenius matrix norm as

$$\dot{\gamma} = 2\|\mathbb{D}\|_F. \quad (2.5)$$

Based on the type of the fluid, various empirical formulae for μ can be employed. In this work, the model proposed by Carreau and Yasuda [1] is used in the form

$$\mu_{CY}(\dot{\gamma}) = \mu_\infty + (\mu_0 - \mu_\infty) [1 + (\lambda \dot{\gamma})^a]^{\frac{n-1}{a}}, \quad (2.6)$$

where μ_0 [$\text{kg m}^{-1} \text{s}^{-1}$] and μ_∞ [$\text{kg m}^{-1} \text{s}^{-1}$] represent dynamic viscosities of Newtonian regimes for $\dot{\gamma} \rightarrow 0+$ and $\dot{\gamma} \rightarrow +\infty$, respectively [1]. Parameters λ [s^{-1}], a , and n are constants determined empirically. The relationship between μ_{CY} and $\dot{\gamma}$ and the two limit viscosities μ_0 and μ_∞ are shown in Figure 2.1. In this study, the following values are used: $\mu_0 = 0.016$ [$\text{kg m}^{-1} \text{s}^{-1}$], $\mu_\infty = 0.0036$ [$\text{kg m}^{-1} \text{s}^{-1}$], $\lambda = 8.2$ [s^{-1}], $a = 0.64$, and $n = 0.2128$.

3. Numerical model. The investigated domain Ω is discretized using a regular lattice $\hat{\Omega}$,

$$\hat{\Omega} = \left\{ \vec{x}_{\vec{i}} = (i\Delta_\ell, j\Delta_\ell) \mid \vec{i} = (i, j), i \in \widehat{N_x - 2}, j \in \widehat{N_y - 2} \right\}, \quad (3.1)$$

where N_x and N_y denote the numbers of discrete lattice sites in x and y directions, respectively, $\Delta_\ell = L_x/N_x = L_y/N_y$, and $\widehat{N} := \{1, 2, \dots, N\}$.

The time interval $(0, T_{fin})$ is equidistantly discretized as $\{t_n \mid t_n = n\Delta_t, n \in \widehat{N_t}\}$, where $N_t + 1$ is the number of time steps and $\Delta_t = T_{fin}/N_t$.

3.1. Lattice Boltzmann method. The lattice Boltzmann method

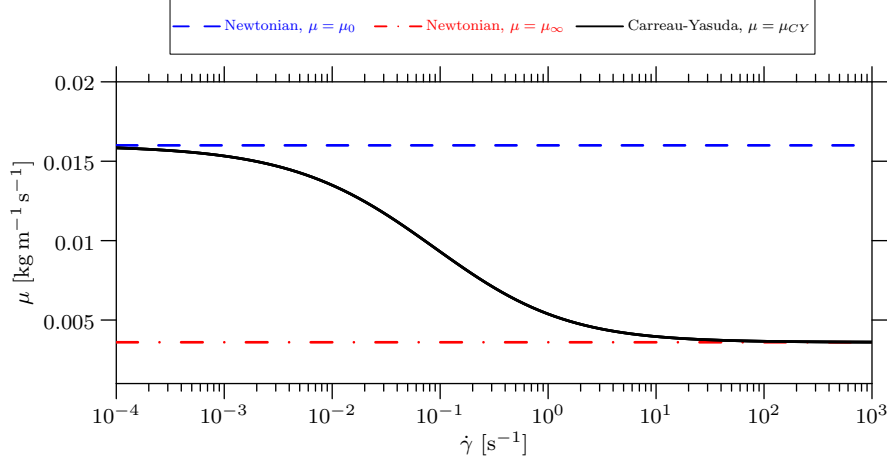


Fig. 2.1: The dependency of the dynamic viscosity on the shear rate given by the Carreau-Yasuda model. The Newtonian limits μ_0 and μ_∞ of the model are marked by the dashed lines.

is a numerical method that uses a mesoscopic description for the solution of the incompressible, Newtonian fluid flow described by Eq (2.4).

The unknowns of the method are the particle density functions f_k , $k \in \hat{q}$, where q denotes the number of directions, in which the density function f_k are propagating within one time step. In this work, we use $q = 9$ in two-dimensional space. In the LBM, it is common to work with non-dimensional quantities, therefore, the functions f_k are considered dimensionless and in order to transform other quantities from physical to non-dimensional units, Δ_ℓ [m] and Δ_t [s] are used as the scaling factors [8, 11].

The evolution of the discrete probability functions is determined $\forall \vec{x}_{\vec{i}} \in \hat{\Omega}$, $\forall t_n \in \hat{N}_t$, $\forall k \in \hat{q}$, by the discrete Boltzmann equation

$$f_k(\vec{x}_{\vec{i}} + \delta_t \vec{\xi}_k, t_n + \delta_t) - f_k(\vec{x}_{\vec{i}}, t_n) = \mathcal{C}_k(\vec{x}_{\vec{i}}, t_n) + \mathcal{G}_k(\vec{x}_{\vec{i}}, t_n), \quad (3.2)$$

where $\delta_t = 1$ is the non-dimensional time step, $\vec{\xi}_k$ [-] is the non-dimensional microscopic velocity,

$$\vec{\xi}_k = \begin{cases} (0, 0)^T & \text{for } k = 1, \\ (1, 0)^T, (0, 1)^T, (-1, 0)^T, (0, -1)^T & \text{for } k = 2, 3, 4, 5, \\ (1, 1)^T, (-1, 1)^T, (-1, -1)^T, (1, -1)^T & \text{for } k = 6, 7, 8, 9. \end{cases} \quad (3.3)$$

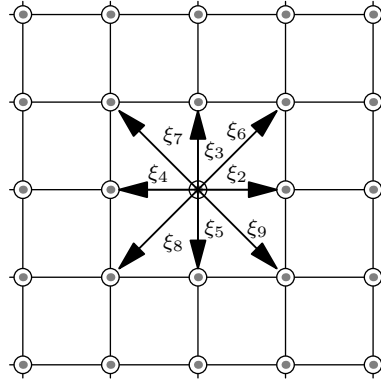


Fig. 3.1: D2Q9 model for $\vec{\xi}_i$, $i \in \hat{9}$.

$\mathcal{C}_k [-]$ is the CLBM discrete collision operator introduced in [6] and $\mathcal{G}_k [-]$ is the discrete source term [12].

Macroscopic dimensionless quantities ρ and \vec{u} are given by

$$\rho = \sum_{k=1}^9 f_k, \quad (3.4a)$$

$$\vec{u} = \frac{1}{\rho} \sum_{k=1}^9 f_k \vec{\xi}_k + \frac{\delta_t}{2} \vec{g}. \quad (3.4b)$$

3.2. Non-Newtonian LBM. Based on [13], the non-Newtonian effects are included into the Newtonian LBM numerical model as follows. Into Eq. (2.4), an additional source term \vec{G} is added which compensates for the non-Newtonian behavior:

$$\rho \left(\frac{\partial \vec{u}}{\partial t} + \vec{u} \cdot \nabla \vec{u} \right) + \nabla p = 2\mu_\infty \nabla \cdot \mathbb{D} + \vec{G} + \rho \vec{g}, \quad (3.5a)$$

where \vec{G} satisfies

$$\vec{G} = 2(\mu_{CY} - \mu_\infty) \nabla \cdot \mathbb{D}. \quad (3.5b)$$

Then, the source term \vec{G} is discretized into the velocity space, i.e., in Eq. (3.2), it is included in \mathcal{G}_k , $k \in \hat{q}$.

4. Results and discussion.

4.1. Mathematical model setup. Flow of a blood-like fluid is considered in a MRI-based, stenosed aorta geometry adapted from [10] and [4], see Figure 4.1. The width (or diameter) of the vessel inside the stenosis (coarctation) is denoted by W [m], see Figure 4.1. The width of a healthy vessel (i.e., without the stenosis) in the middle of the computational domain is denoted by W_0 . In order to investigate the non-Newtonian effects in the cases of more and less severe stenosis, the adopted geometry is modified using gradually decreasing values of W . Specifically, the results for these three aorta geometries are presented in this section: (a) original geometry adapted from [10, 4] with $W \approx \frac{1}{2}W_0$, (b) geometry with $W = \frac{1}{3}W_0$, and (c) geometry with $W = \frac{1}{4}W_0$.

In order to minimize the influence of the inflow and outflow boundary condition, the investigated domain was prolonged as illustrated in Figure 4.1. For all simulations, a single computational lattice is used with $N_x = 1280$ and $N_y = 256$. Thus, the spatial and temporal step sizes are $\Delta_\ell = 0.15$ mm and $\Delta_t = 2.11 \cdot 10^{-7}$ s, respectively. A fully developed velocity profile between two parallel plates is prescribed at the inlet boundary Γ_{in} . The maximal velocity of 1.5 ms⁻¹ corresponds to the blood velocity in human arterial vessels. At Γ_{out} , the free outflow boundary condition is prescribed. At walls that are represented by the gray area in Figure 4.1, the no-slip boundary condition is prescribed.

4.2. Temporal and spatial averaging. To illustrate the differences between the Newtonian and non-Newtonian fluid flow, three quantities – the velocity magnitude; the negative horizontal flux; and the difference between the non-Newtonian

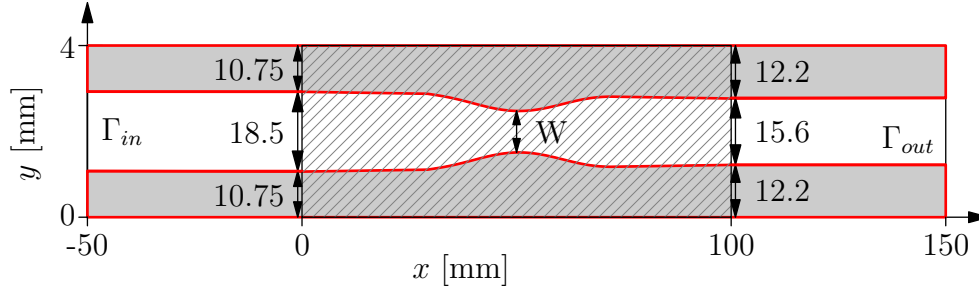


Fig. 4.1: Schematic representation of the computational domain with dimensions marked in millimeters. The hatched area represents the domain of interest $\Omega = (0, 100) \times (0, 40)$. At Γ_{in} and Γ_{out} , the inflow and free outflow boundary conditions are prescribed, respectively. The gray area represents the region outside vessels which behaves as impermeable wall in the numerical simulations.

viscosity μ_{CY} and the Newtonian viscosity μ_{∞} – are averaged over the time interval (t_1, t_2) using the formula

$$\bar{Q} = \frac{1}{t_2 - t_1} \sum_{t_n=t_1}^{t_2} Q(t_n), \quad (4.1)$$

where t_n is the discrete time and Q represents the time-averaged quantity in question. In all cases, $t_1 = 2$ and $t_2 = 20$ s were used.

In order to illustrate the backward velocity flux as in [5], space averaging over vertical axis is done using the formula

$$\langle Q \rangle (x) = \frac{1}{A(x)} \int_{A(x)} Q(x, y) dy, \quad (4.2)$$

where Q represents the space-averaged quantity and $A(x)$ is the cross section area of the vessel at x . Finally, the space- and time- averaged quantity Q is denoted by $\langle \bar{Q} \rangle$.

4.3. Results. The time integrated quantities, referred to as the mean velocity magnitude, the mean negative horizontal flux and the mean viscosity difference, are shown in Figures 4.2, 4.3, and 4.5, respectively.

The difference in the mean velocity magnitude, computed by the Newtonian models with $\mu = \mu_0$ and $\mu = \mu_{\infty}$, and the non-Newtonian Carreau-Yasuda model, is insignificant in the case of the least severe stenosis as shown in Figure 4.2a-c. In the case of more severe stenosis, the models provide slightly different results in terms of mean velocity magnitudes as shown in Figure 4.2d-i. The most different case is for $\mu = \mu_0$, where the steady state in the integrated mean velocity was not reached.

In order to better quantify the effects of the Carreau-Yasuda model compared to two Newtonian models, the backflow caused by turbulence is investigated by means of the mean negative horizontal flux in the region behind the coartcation, see Figures 4.3 and 4.5. For the least stenosed artery, the Newtonian model with $\mu = \mu_0$ predicts smaller negative flux than the Newtonian model with $\mu = \mu_{\infty}$ and Carreau-Yasuda model, as shown in the first row of figures in Figure 4.3 and in Figure 4.4a. It can be concluded that for all cases, the Newtonian model with $\mu = \mu_{\infty}$ is a sufficiently good approximation of the non-Newtonian Carreau-Yasuda model.

To illustrate the origin of different backflow magnitudes observed in Figure 4.4, the difference between μ_{CY} , μ_0 , and μ_∞ is shown in Figure 4.5. As expected, for highly stenosed vessels, the blood flow velocity inside and behind the stenosis increases and as turbulence occurs in the flow, $\dot{\gamma}$ becomes large, and, therefore, the viscosity μ_{CY} decreases towards μ_∞ . Even if the flow remains almost laminar for the case of $W \approx \frac{1}{2}W_0$, $\dot{\gamma}$ is not zero (as shown by variable viscosity behind the stenosis in Figure 4.5a), and again, the Newtonian results with $\mu = \mu_\infty$ correspond better to μ_{CY} than the Newtonian results with $\mu = \mu_0$.

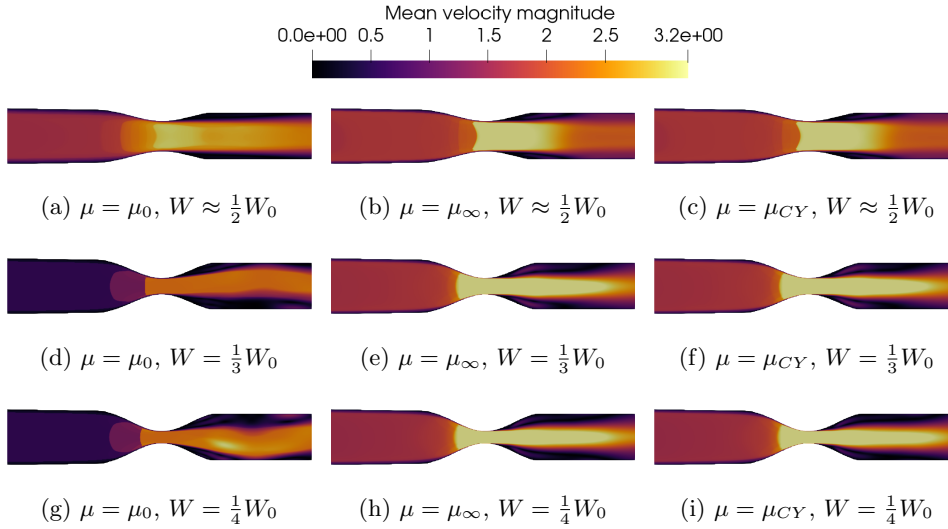


Fig. 4.2: Magnitudes of mean velocity for gradually decreasing values of W . Results for the Newtonian models with $\mu = \mu_0$ and $\mu = \mu_\infty$ are shown in first two columns and for the non-Newtonian Carreau-Yasuda model, the results are shown in the last column.

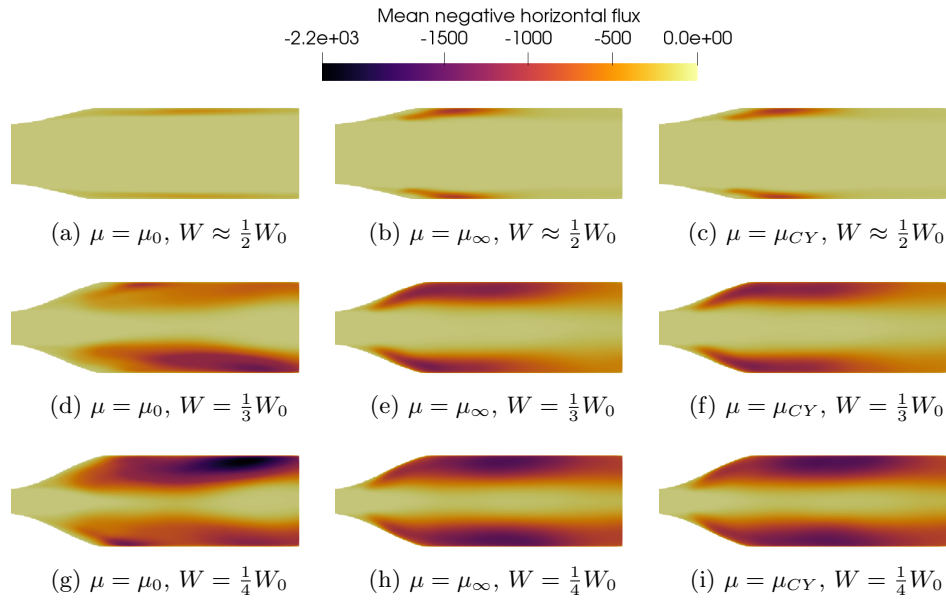


Fig. 4.3: Comparison of mean negative horizontal flux $\overline{\rho u_x}$ behind the vessel stenosis for gradually decreasing values of W . Results for the Newtonian models with $\mu = \mu_0$ and $\mu = \mu_\infty$ are shown in first two columns and for the non-Newtonian Carreau-Yasuda model, results are shown in the last column.

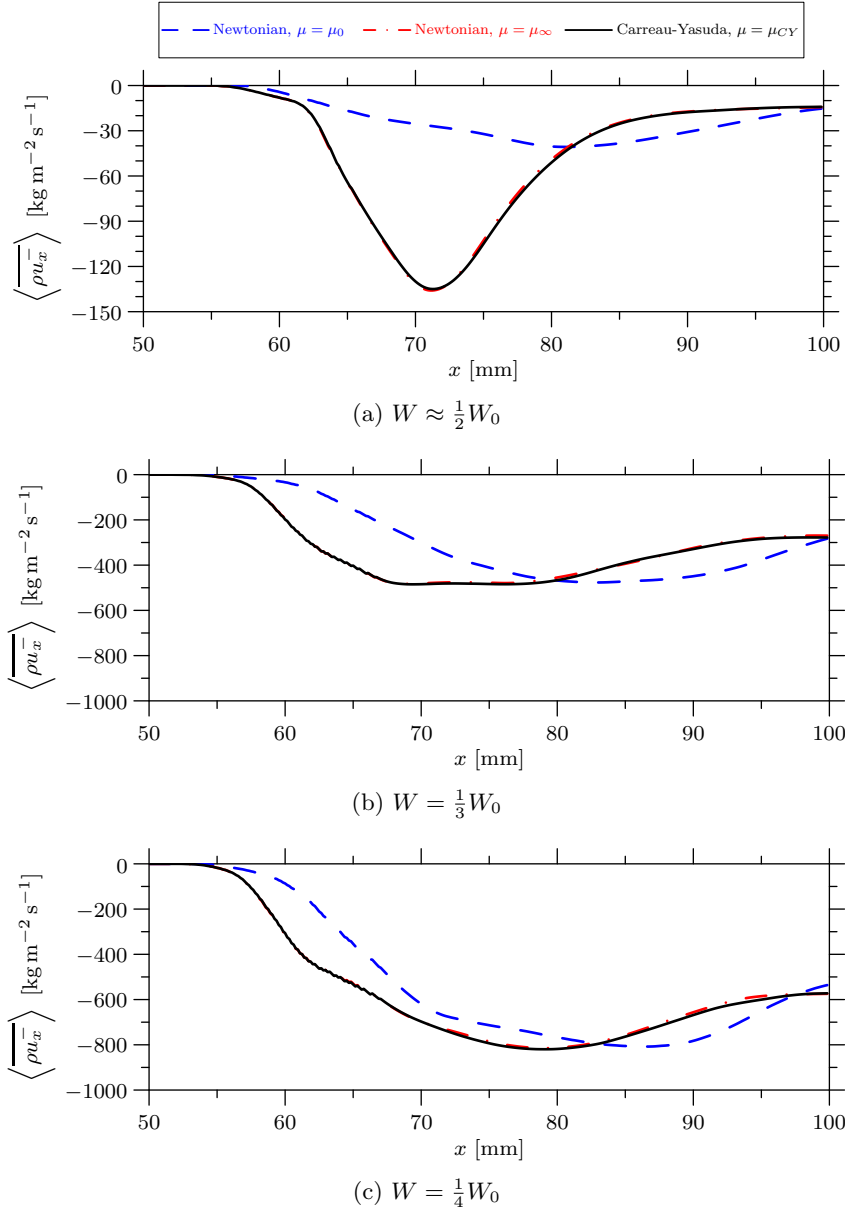


Fig. 4.4: Comparison of space- and time- averaged negative horizontal fluxes $\langle \overline{\rho u_x} \rangle$ behind the stenosis for gradually decreasing values of W .

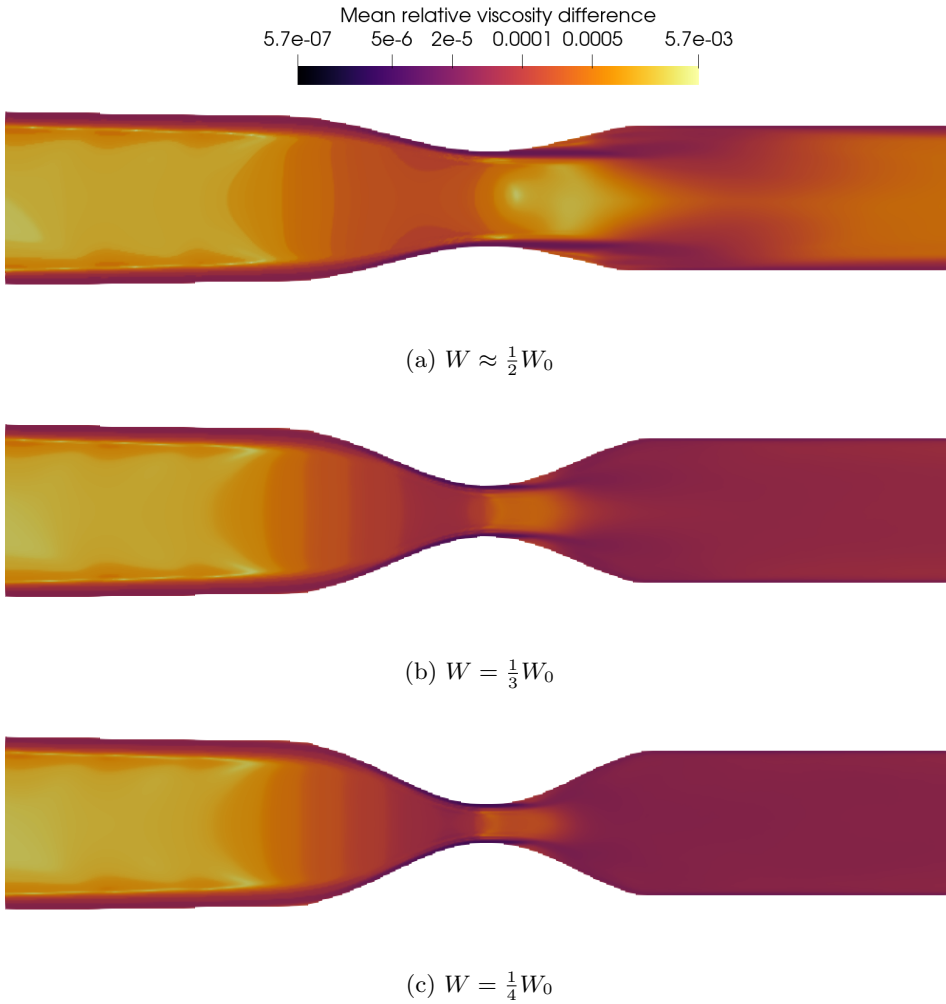


Fig. 4.5: Mean relative difference between μ_{CY} and μ_∞ defined by $\frac{\mu - \mu_\infty}{\mu_0 - \mu_\infty}$ in logarithmic scale for gradually decreasing values of W .

5. Conclusion. The impact of non-Newtonian properties in the mathematical modelling of fluid flow in stenosed arteries was investigated in order to determine whether the Newtonian model is a feasible approximation, or it is necessary to use a non-Newtonian model. Using three aorta geometries with gradually increasing severities of stenosis, the comparison of Carreau-Yasuda model and two Newtonian models for the Carreau-Yasuda limit viscosities μ_0 and μ_∞ showed that the severity of stenosis has a non-negligible impact on the fluid viscosity in the region behind the stenosis. The fluid viscosity behind the stenosis decreases with a decreasing width of

the stenosis due to turbulence. Consequently, the lower fluid viscosity in this region leads to a larger negative horizontal flux that can potentially distort MRI measurements. For the least stenosed artery, the variations in the fluid viscosity values are smaller, nevertheless, the negative horizontal flux is affected by the viscosity value of the two limiting Newtonian regimes of the Carreau-Yasuda model. In the case of most stenosed artery this dependence is less significant. Based on the performed computational experiments, it can be concluded that the Newtonian approach is applicable for the geometries of large vessels, however, with a careful choice of the Newtonian fluid viscosity.

Acknowledgments. The work was supported by the Czech Science Foundation project No. 18-09539S, by the project No. NV19-08-00071 of the Ministry of Health of the Czech Republic, by the Ministry of Education, Youth and Sports of the Czech Republic under the OP RDE grant number CZ.02.1.01/0.0/0.0/16_019/0000778 Centre for Advanced Applied Sciences, and by the Grant Agency of the Czech Technical University in Prague, grant No. SGS20/184/OHK4/3T/14.

REFERENCES

- [1] J. Boyd, J. M. Buick, and S. Green. Analysis of the Casson and Carreau-Yasuda non-Newtonian blood models in steady and oscillatory flows using the lattice Boltzmann method. *Physics of Fluids*, 19(9):093103, 2007.
- [2] S.S. Chikatamarla, S. Ansumali, and I. V. Karlin. Entropic lattice Boltzmann models for hydrodynamics in three dimensions. *Physical review letters*, 97(1):010201, 2006.
- [3] D. d’Humières. Generalized lattice-Boltzmann equations. *Rarefied gas dynamics*, 1992.
- [4] R. Fučík, P. Eichler, R. Straka, P. Pauš, J. Klinkovský, and T. Oberhuber. On optimal node spacing for immersed boundary–lattice Boltzmann method in 2D and 3D. *Computers & Mathematics with Applications*, 77(4):1144–1162, 2019.
- [5] R. Fučík, R. Galabov, P. Pauš, P. Eichler, J. Klinkovský, R. Straka, J. Tintěra, and R. Chabinok. Investigation of phase-contrast magnetic resonance imaging underestimation of turbulent flow through the aortic valve phantom: Experimental and computational study using lattice Boltzmann method. *Magnetic Resonance Materials in Physics, Biology and Medicine*, pages 1–14, 2020.
- [6] M. Geier, A. Greiner, and J. G. Korvink. Cascaded digital lattice Boltzmann automata for high Reynolds number flow. *Physical Review E*, 73(6):066705, 2006.
- [7] M. Geier, A. Pasquali, and M. Schönherr. Parametrization of the cumulant lattice Boltzmann method for fourth order accurate diffusion Part I: Derivation and validation. *J. Comput. Phys*, 348:862–888, 2017.
- [8] Z. Guo and C. Shu. *Lattice Boltzmann method and its applications in engineering*, volume 3. World Scientific, 2013.
- [9] Payne Stephen J. *Cerebral Blood Flow and Metabolism: A Quantitative Approach*. World Scientific, 2017.
- [10] Y. Kim, S. Lim, S. V. Raman, O. P. Simonetti, and A. Friedman. Blood flow in a compliant vessel by the immersed boundary method. *Annals of biomedical engineering*, 37(5):927–942, 2009.
- [11] T. Krüger, H. Kusumaatmaja, A. Kuzmin, O. Shardt, G. Silva, and E. M. Viggien. *The Lattice Boltzmann Method*. Springer, 2017.
- [12] K. N. Premnath and S. Banerjee. Incorporating forcing terms in cascaded lattice Boltzmann approach by method of central moments. *Physical Review E*, 80(3):036702, 2009.
- [13] C.-H. Wang and J.-R. Ho. A lattice Boltzmann approach for the non-Newtonian effect in the blood flow. *Computers & Mathematics with Applications*, 62(1):75–86, 2011.